

# Long-range model of vibrational autoionization in core-nonpenetrating Rydberg states of NO

Timothy J. Barnum,<sup>1, a)</sup> Gloria Clausen,<sup>2</sup> Jun Jiang,<sup>1, b)</sup> Stephen L. Coy,<sup>1</sup> and Robert W. Field<sup>1, c)</sup>

<sup>1)</sup>Department of Chemistry, Massachusetts Institute of Technology, Cambridge, Massachusetts 02139, USA

<sup>2)</sup>Laboratorium für Physikalische Chemie, ETH Zürich, Vladimir-Prelog-Weg 2, 8093 Zürich, Switzerland

(Dated: 8 March 2022)

In high orbital angular momentum ( $\ell \geq 3$ ) Rydberg states, the centrifugal barrier hinders close approach of the Rydberg electron to the ion-core. As a result, these *core-nonpenetrating* Rydberg states can be well described by a simplified model in which the Rydberg electron is only weakly perturbed by the long-range electric properties (i.e., multipole moments and polarizabilities) of the ion-core. We have used a long-range model to describe the vibrational autoionization dynamics of high- $\ell$  Rydberg states of nitric oxide (NO). In particular, our model explains the extensive angular momentum exchange between the ion-core and Rydberg electron that had been previously observed in vibrational autoionization of *f* ( $\ell = 3$ ) Rydberg states. These results shed light on a long-standing mechanistic question around these previous observations, and support a direct, vibrational mechanism of autoionization over an indirect, predissociation-mediated mechanism. In addition, our model correctly predicts newly measured total decay rates of *g* ( $\ell = 4$ ) Rydberg states because, for  $\ell \geq 4$ , the non-radiative decay is dominated by autoionization rather than predissociation. We examine the predicted  $\text{NO}^+$  ion rotational state distributions generated by vibrational autoionization of *g* states and discuss applications of our model to achieve quantum state selection in the production of molecular ions.

## I. INTRODUCTION

Among the most compelling new topics at the intersection of chemistry and physics is the study of chemical reactions and molecular collisions at extremely cold temperatures in which quantum state behavior is resolved.<sup>1–3</sup> A diverse range of experimental techniques encompassing beams, traps, and cryogenic matrices now enable study of collision energies from a few K to sub-mK (see Ref. 3 and references therein). Beyond control of the collision energy, resolution of individual quantum states in both reactants and products has led to some of the most detailed pictures of chemical reactions to date.<sup>4,5</sup> In such quantum-state-resolved studies of chemical reactivity, the generation of reactant molecules or ions in single quantum states is one of the greatest challenges and only a few systems have been experimentally realized thus far.<sup>6,7</sup>

One approach to the preparation of quantum-state-selected samples is to selectively excite a Rydberg state of a neutral molecule, which then autoionizes to produce a molecular ion in the desired quantum state. Autoionization refers to the spontaneous ionization of a neutral Rydberg molecule when the total energy of a Rydberg electron around a vibrationally excited ion-core exceeds the ionization energy of the vibrationless level in one or more rotational states. Naively, this process would be expected

to leave the ion-core rotational state unchanged because of the mismatch of vibronic and rotational time scales. However, in recent applications, this approach has only succeeded in producing molecular ions distributed over at least three final rotational states.<sup>8,9</sup> Indeed, earlier work demonstrated that rotational quantum number changes as large as four quanta are possible in the autoionization of certain Rydberg series,<sup>10,11</sup> upending the simple picture of the Rydberg electron being released without perturbation of the ion-core.

In a series of pioneering experiments on the Rydberg states of nitric oxide (NO), the Zare group<sup>10–13</sup> employed photoelectron spectroscopy to examine the  $\text{NO}^+$  ion rotational state distributions following vibrational autoionization of a selected Rydberg state. In nearly all cases, the autoionization of *s*, *p*, and *f* Rydberg states of NO resulted in extensive angular momentum exchange between the Rydberg electron and the ion-core. Moreover, the observation of both even and odd parity final rotational states implied ejection of the Rydberg electron with both even and odd values of  $\ell$ , a surprising result in light of the small dipole moment of NO which induces only weak interactions between Rydberg series of even and odd  $\ell$ .<sup>14–16</sup> It was concluded that at least two mechanisms were required to explain this new data: (1) direct coupling of the bound Rydberg state to even- and odd- $\ell$  channels in the ionization continuum by vibrationally dependent matrix elements and (2) indirect, electronic coupling to the ionization continuum through dissociative valence states.<sup>11</sup> A later study<sup>17</sup> suggested that the indirect coupling mechanism alone could explain the production of both even- and odd- $\ell$  photoelectrons as a result of the strong Rydberg-valence coupling responsible for the rapid predissociation of most NO Rydberg states.

<sup>a)</sup>Electronic mail: tbarnum@mit.edu

<sup>b)</sup>Present address: Lawrence Livermore National Laboratory, 7000 East Avenue, Livermore, California 94550, USA

<sup>c)</sup>Author to whom correspondence should be addressed: rfield@mit.edu

To date, no quantitative theory has accounted for the mechanisms operative in NO.

In the present work, we apply a long-range model of vibrational autoionization to explain the dynamics of  $f$  ( $\ell = 3$ ) and  $g$  ( $\ell = 4$ ) Rydberg states of NO. The model relies on the simplifying assumption that the interaction of the Rydberg electron with the ion-core occurs only at long range via the electric properties of the ion-core.<sup>18,19</sup> This assumption explicitly limits the applicability of the long-range model to *core-nonpenetrating* Rydberg states: states with sufficiently high  $\ell$  (typically,  $\ell \geq 3$ ) such that the Rydberg electron has minimal overlap with the spatial region of the ion-core. In spite of its simplicity, this model accounts for the majority of observed rotational decay channels following autoionization of  $f$  states, providing explicit support for the proposed direct, vibrational autoionization mechanism.

In addition, we have measured total decay rates for autoionizing  $g$  levels and find good agreement between those measurements and our model predictions of autoionization rates in the absence of predissociation. The success of our long-range model in explaining these experimental results has led us to a theoretical examination of the rotational state distribution of autoionizing  $g$  Rydberg states. We find production of a single (>90%) rotational state of the  $\text{NO}^+$  ion is possible through autoionization of specific  $g$  Rydberg states. We discuss how this universal predissociation-free behavior of high- $\ell$  Rydberg states may be used for optimally state-selective production of molecular ions for cutting-edge applications in molecular physics and cold chemistry.

## II. THEORETICAL AND COMPUTATIONAL METHODS

The physical basis of long-range autoionization in molecular Rydberg states has been described previously,<sup>18,19</sup> and only a brief summary is presented here. The autoionization rate can be obtained from Fermi's golden rule:

$$\Gamma = \frac{2\pi}{n^3} |\langle \Phi_f | \mathbf{H}' | \Psi_i \rangle|^2 \quad (1)$$

where  $\mathbf{H}'$  is the Hamiltonian that describes all long-range interactions,  $\Phi_f$  is the final continuum state, and  $\Psi_i$  is the initial Rydberg state. In the results presented here, we explicitly consider contributions from the dipole moment, quadrupole moment, and dipole-dipole polarizability of the  $\text{NO}^+$  ion-core:

$$\mathbf{H}' = \mathbf{H}_{\text{dipole}} + \mathbf{H}_{\text{quad}} + \mathbf{H}_{\text{pol}} \quad (2)$$

The initial Rydberg state is specified by quantum numbers for the vibrational state of the ion-core ( $v$ ), the rotational state of the ion-core ( $R$ ), the principal quantum number ( $n$ ), the Rydberg electron orbital angular momentum ( $\ell$ ), and the total angular momentum ( $N$ ) and its space-fixed projection ( $M$ ). The final continuum state

is specified by the vibrational ( $v^+$ ) and rotational ( $N^+$ ) quantum numbers for the bare ion, the energy above threshold ( $\epsilon$ ) and orbital angular momentum ( $\ell'$ ) of the electron, and the total angular momentum of the system ( $N'$ ) and its space-fixed projection ( $M'$ ). Selection rules for all such interaction mechanisms require  $N' = N$  and  $M' = M$ . All matrix elements can be computed following the method of Eyler and Pipkin.<sup>20</sup> For example, the multipolar interaction of rank  $k$  has the form:

$$\begin{aligned} & \langle v^+ N^+ \epsilon \ell' N' M' | \mathbf{H}_k | v R n \ell N M \rangle \\ &= -e \langle v^+ N^+ | Q_k(z) | v R \rangle \langle \epsilon \ell' | r^{-(k+1)} | n \ell \rangle \\ & \quad \times \delta_{N', N} \delta_{M', M} (-1)^{\ell + \ell' + N} \\ & \quad \times [(2\ell' + 1)(2\ell + 1)(2N^+ + 1)(2R + 1)]^{1/2} \\ & \quad \times \begin{Bmatrix} N & N^+ & \ell' \\ k & \ell & R \end{Bmatrix} \begin{pmatrix} \ell' & k & \ell \\ 0 & 0 & 0 \end{pmatrix} \begin{pmatrix} N^+ & k & R \\ 0 & 0 & 0 \end{pmatrix} \quad (3) \end{aligned}$$

The selection rules for changes in the rotational ( $R$  and  $N^+$ ) and orbital ( $\ell$  and  $\ell'$ ) angular momentum quantum numbers are determined by the Wigner 3-j symbols. For the mechanisms considered in our model:

dipole:  $\Delta\ell = \pm 1; N^+ - R = \pm 1$

quadrupole:  $\Delta\ell = 0, \pm 2; N^+ - R = 0, \pm 2$

isotropic polarizability:  $\Delta\ell = 0; N^+ - R = 0$

anisotropic polarizability:  $\Delta\ell = 0, \pm 2; N^+ - R = 0, \pm 2$

In Equation 3,  $Q_k(z)$  represents the  $k^{\text{th}}$  multipole moment of the ion-core as a function of the internuclear distance  $z$ . In the harmonic approximation, interactions via this term are dominated by changes of  $\Delta v = -1$ . We have calculated the potential energy curve (PEC) and the electric properties of the  $\text{NO}^+$  ion as a function of internuclear distance using the ORCA program suite.<sup>21,22</sup> Geometry optimization calculations at 0.1 a.u. intervals in the region of the equilibrium internuclear distance were performed employing the Complete Active Space Self Consistent Field (CASSCF) method, followed by N-valence electron perturbation theory (NEVPT2) with the aug-cc-pVQZ basis set. The use of NEVPT2 to capture dynamical correlation effects significantly improved the PEC of  $\text{NO}^+$  relative to a previously reported calculation.<sup>23</sup> Vibrational wave functions were computed on this PEC by a 1-D Discrete Variable Representation (DVR) scheme<sup>24</sup> and used to calculate the matrix elements for electric properties.

The second term in Equation 3 involves radial electronic wavefunctions for both the bound  $|n\ell\rangle$  and continuum  $|\epsilon\ell\rangle$  states of the Rydberg electron. These were assumed to be hydrogenic and were generated numerically by Numerov integration on the Coulomb potential using square-root scaling of the radial distance  $r$  from the ion-core.<sup>25</sup> The continuum wavefunctions were normalized to the value of the analytic wavefunction at the position of

its first maximum computed using the generalized hypergeometric function implemented in the MATLAB software package.

In calculating total autoionization rates, interference effects between the various long-range mechanisms are considered by summing the amplitudes of the different mechanisms before computing the autoionization rate according to Equation 1. Since different final rotational states of the ion represent physically distinct decay channels, we can compute the autoionization yield of a particular ion rotational state by summing over the autoionization rates for all values of the final electron angular momentum  $\ell'$ . Our treatment neglects interference among outgoing electron partial waves with different values of  $\ell'$  and thus the photoelectron angular distributions are not accessible by our calculations. This limitation results in a quantitatively inexact comparison between our theoretical results and some of the experimental photoelectron spectroscopy results,<sup>10,11</sup> as discussed below.

Throughout this work, we specify individual Rydberg states using the compact notation  $n\ell R_N$ , where the quantum numbers are defined as above. In some cases, it is convenient to specify a particular electric fine structure component by the label  $\ell_R = N - R$  rather than  $N$ , in order to compare the behavior of Rydberg states with different values of the core rotation.

### III. EXPERIMENTAL METHODS

As an additional point of validation for our theoretical results, we sought to measure the total decay rates of  $g$  series Rydberg states. Rydberg states with  $\ell = 4$  must be accessed via an intermediate state with  $\ell = 3$  due to a  $\Delta\ell = \pm 1$  selection rule for transitions between high- $\ell$  molecular Rydberg states. For NO, we employed a previously described triple resonance excitation scheme that uses the A  $^2\Sigma^+$  and 4f levels as intermediate states.<sup>26</sup> The laser radiation for the triple resonance excitation scheme was generated by three pulsed dye laser systems. The third harmonic (355 nm) of a pulsed Nd:YAG laser (Spectra Physics GCR 270) pumped two pulsed dye lasers (SIRAH Cobra Stretch, Lambda Physik Scanmate 2E), both operated with Stilbene 420 dye. The output of the SIRAH dye laser was frequency doubled in a  $\beta$ -barium borate crystal to generate the radiation around 217 nm appropriate for pumping rotational transitions in the A  $^2\Sigma^+ \leftarrow$  X  $^2\Pi_{1/2}$  (1,0) band. The fundamental output of the Lambda Physik dye laser in the 420 nm region was resonant with transitions in the 4f  $\leftarrow$  A  $^2\Sigma^+$  (1,1) band. The intensity for this transition is derived from the partial  $d$  ( $\ell = 2$ ) character of the A  $^2\Sigma^+$  state, as discussed previously.<sup>16</sup> The IR radiation around 1500 nm needed to drive ng  $\leftarrow$  4f transitions was generated by a third pulsed dye laser (Continuum ND6000), operated with DCM dye and pumped by the second harmonic (532 nm) of a pulsed Nd:YAG laser (Spectra Physics Pro 270). The output of this dye laser was then mixed with

the fundamental (1064 nm) of the same Nd:YAG laser in a LiNbO<sub>3</sub> crystal to produce IR radiation by difference frequency generation. All three laser beams were overlapped with dichroic mirrors and loosely focused into the detection chamber.

We measured the total decay rates of  $g$  ( $v = 1$ ) Rydberg states, over a range of values of  $n$ ,  $R$ , and  $\ell_R$ , by delayed pulsed field extraction of NO<sup>+</sup> ions resulting from autoionization. The ion detection apparatus has been described in detail previously<sup>27</sup> and only relevant details are given here. NO gas seeded at 0.5 % in Ar was expanded through a pulsed valve (General Valve Series 9,  $d = 1$  mm) and passed through a conical skimmer ( $d = 0.5$  mm) before entering the differentially pumped detection chamber that contains a Wiley-McLaren type time-of-flight mass spectrometer. The molecular beam was crossed at right angles by the three excitation lasers. By strongly attenuating the first and second lasers and adding 10 ns delays between each of the laser pulses, the ion signal due to multiphoton ionization was minimized. Following a variable delay time after the third laser pulse, a pulsed field of 200 V/cm was applied to the bottom electrode and ions produced by vibrational autoionization were accelerated through a 75 cm field-free region and impinged on a multichannel plate detector. The pulsed field was weaker than that required to field-ionize the Rydberg states investigated in this work. An exponential function was fit to the raw ion yield data starting approximately 10 ns after the first appearance of ions to minimize the influence of the extraction field rise time.

Two experimental effects can interfere with the described measurements. First, stray electric fields can mix  $g$  states with high- $\ell$  Rydberg states. This results in lengthened lifetimes relative to those in field-free conditions.<sup>28,29</sup> We estimate the stray electric field in our apparatus by measuring the 44h  $\leftarrow$  43g transition at approximately 80 GHz by broadcasting a weak microwave field into the detection region following laser population of the initial 43g state. Based on the observed line broadening, we estimate the presence of a stray electric field of approximately 90 mV/cm in the apparatus during these experiments. We performed a Stark effect calculation analogous to that presented by Vrakking.<sup>30</sup> With this stray electric field, we found that, for the highest  $n$  values investigated ( $n = 28$ ), the purity of all states was greater than 97% and the lifetimes were altered by less than 3% relative to those of the field-free states. Moreover, we observed no deviation from the expected  $n^3$  scaling of the lifetime for different  $n$  values.

Second, the laser linewidth in the final excitation step of our experiment was approximately 0.05 cm<sup>-1</sup>, substantially larger than the electric fine structure splitting of the  $g$  Rydberg states. For some levels (ng0<sub>4</sub>, ng1<sub>3</sub>, ng2<sub>2</sub>, and ng3<sub>1</sub>), we could unambiguously excite each of these selected electric fine structure components by appropriate selection of the intermediate levels. For all other levels where perfect fine structure selection was

not possible, we took advantage of a strong  $\Delta N = +1$  propensity rule in the final step of the excitation scheme, which involves a  $\Delta \ell = +1$  transition. Thus, by careful selection of the intermediate state we could *predominantly* excite a single  $\ell_R$  component of the Rydberg state despite our inability to resolve individual states. We determined the anticipated purity of the final state preparation by explicitly calculating the triple-resonance transition intensities. Following the procedure of Petrović and Field,<sup>31</sup> we first calculated the transition intensity for each step in a Hund's case (a) basis and then performed a rotational frame transformation to the correct Hund's case for each level. This treatment, which explicitly considers the summation over unresolved spin doublets, has previously been shown to predict accurate relative intensities in multiple resonance experiments.<sup>31</sup>

In Table I, we summarize the excitation schemes and the calculated selectivity for every level investigated in this work. For the majority of states, very high purity of the desired state is predicted. However, the selectivities for  $ng3_2$ ,  $ng3_3$ , and  $ng3_5$  states are only 0.63, 0.61, and 0.72, respectively. The majority of the contamination in this preparation scheme is from the unresolved Q-type transition to the electric fine structure component with total angular momentum  $N - 1$  relative to the desired  $N$  level. In spite of this contamination, it is evident from the results presented in Figure 5 and discussed later in the text, that these less-perfectly selected states do not exhibit greater discrepancies from the calculation than the other data. This may simply be a result of the modest variation in rates expected among the different  $\ell_R$  states, so that contamination of the desired state preparation by a neighboring state will not dramatically alter the measured rates.

#### IV. RESULTS AND DISCUSSION

##### A. Rotational state distributions from autoionization of $f$ Rydberg states

We calculated the  $\text{NO}^+$  ion rotational state distributions that result from vibrational autoionization of selected  $f$  Rydberg states by summing the rates of all outgoing electron partial waves that result in formation of a given final rotational state of the ion. The model predictions are compared to the experimental results for  $v = 1$ <sup>10,11</sup> and  $v = 2$ <sup>13</sup>  $f$  Rydberg states. Briefly, these experiments prepared a selected  $f$  Rydberg state by double resonance excitation of  $\text{NO}$  in a molecular beam. Vibrational autoionization of these Rydberg states occurred under field-free conditions in a time-of-flight photoelectron spectrometer. The energy resolution of the spectrometer was sufficient to resolve individual ion rotational levels for rotational quantum numbers  $N^+ \gtrsim 13$ . The laser resolution was insufficient to selectively prepare individual  $\ell_R$  components of a Rydberg complex, resulting in simultaneous excitation of as many as three  $\ell_R$

TABLE I. Excitation scheme and selectivity for preparation of the indicated Rydberg state. In all cases, a final R-type transition to the desired  $N$  level is the most intense line. Nearly all contamination is due to a Q-type transition to the  $N - 1$  component. The  $A \leftarrow X$  transitions are labeled as  $\Delta J_{F_{1/2}F_{1/2'}}$  where the number subscripts indicate a transition between the  $F_1$  spin component of the  $X$  state, namely  $X^2\Pi_{1/2}$  levels, and the  $F_1$  or  $F_2$  spin component of the  $A$  state, namely  $J = N + 1/2$  or  $J = N - 1/2$  levels with the same value of  $N$ .<sup>32</sup> The  $4f \leftarrow A$  transitions are labeled as  $^{R-N'}\Delta N_{\ell_R}$  where  $N'$  is the total angular momentum excluding spin of the  $A$  state level.<sup>16</sup>

| State   | $A \leftarrow X$ | $4f \leftarrow A$ | Selectivity |
|---------|------------------|-------------------|-------------|
| $ng0_4$ | $R_{21}(0.5)$    | $^{-2}R_3(2)$     | 1.0         |
| $ng1_3$ | $P_1(2.5)$       | $^0R_1(1)$        | 1.0         |
| $ng1_4$ | $R_{21}(1.5)$    | $^{-2}Q_2(3)$     | 0.976       |
| $ng1_5$ | $R_{21}(1.5)$    | $^{-2}R_3(3)$     | 0.988       |
| $ng2_2$ | $P_1(1.5)$       | $^2R_{-1}(0)$     | 1.0         |
| $ng2_3$ | $R_{21}(0.5)$    | $^0Q_0(2)$        | 0.959       |
| $ng2_4$ | $R_{21}(0.5)$    | $^0R_1(2)$        | 0.965       |
| $ng2_5$ | $R_{21}(2.5)$    | $^{-2}Q_2(4)$     | 0.920       |
| $ng2_6$ | $R_{21}(2.5)$    | $^{-2}R_3(4)$     | 0.972       |
| $ng3_1$ | $P_1(2.5)$       | $^2P_{-3}(1)$     | 1.0         |
| $ng3_2$ | $P_1(2.5)$       | $^2Q_{-3}(1)$     | 0.626       |
| $ng3_3$ | $R_{21}(1.5)$    | $^0P_{-1}(3)$     | 0.614       |
| $ng3_5$ | $R_{21}(3.5)$    | $^{-2}P_1(5)$     | 0.724       |
| $ng3_6$ | $R_{21}(3.5)$    | $^{-2}Q_2(5)$     | 0.872       |
| $ng3_7$ | $R_{21}(3.5)$    | $^{-2}R_3(5)$     | 0.955       |

components. In most cases, photoelectron spectra were observed at a single angle between the time-of-flight axis and the polarization direction of the laser beams. In a few cases for  $v = 2$  Rydberg states, the extreme  $\ell_R$  components ( $\ell_R = \pm 3$ ) were selectively excited by utilizing circularly polarized laser light.<sup>13</sup> In those cases, complete photoelectron angular distributions were also collected by observing the photoelectron spectra at several angles between the time-of-flight axis and the laser polarization axis. For both the  $v = 1$  and  $v = 2$  data sets, we examined only the  $\Delta v = -1$  autoionization channel. The much slower  $\Delta v = -2$  decay is likely contaminated by additional mechanisms such as the predissociation-mediated autoionization considered previously.<sup>33</sup> The results presented here may assist in future work on disentangling the multiple autoionization mechanisms for  $|\Delta v| > 1$  decay. To clarify the distinction between the quantum numbers of the ion-core and the bare ion, we refer to the rotational quantum number of the ion-core as  $R$  and the bare ion rotational quantum number as  $N^+$ , which is identical to the total angular momentum for the  $^1\Sigma^+$  ground electronic state of  $\text{NO}^+$ .

Figure 1 shows a comparison between the experimental data and our model predictions for the  $13f16_{15,16,17}$  ( $v = 2$ ) states. These three electric fine structure states have  $\ell_R$  values of  $-1, 0$ , and  $1$ . The relative intensities of

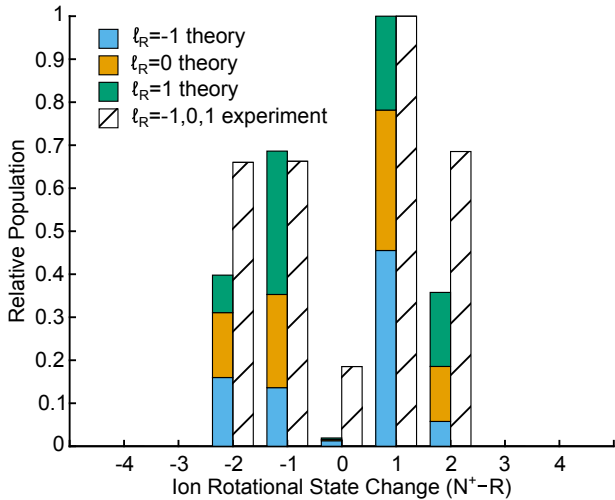


FIG. 1. Rotational state distribution following vibrational autoionization of the unresolved  $13f16_{15,16,17}$  ( $v = 2$ ) states. The experimental data (hatched bars) are the photoelectron peak intensities observed at one angle, and serve as proxies for the true  $\text{NO}^+$  ion rotational state distribution. The theoretical predictions appear as stacked bars in blue, orange, and green for the  $\ell_R = -1, 0$ , and 1 states, respectively. Both data sets have been normalized by setting the most intense peak to 1. The long-range model predicts intensity in all five experimentally observed decay channels.

the observed photoelectron peaks at energies corresponding to the given change of rotational state ( $N^+ - R$ ) are shown as hatched bars. The model predictions are shown as blue, orange, and green stacked bars for the  $\ell_R = -1, 0$ , and 1 states, respectively. It is important to note that the intensity of the photoelectron peak observed at a single angle does not precisely represent the yield for that rotational channel. The total yield is given by the photoelectron intensity summed over the full photoelectron angular distribution. The long-range model could be extended to predict photoelectron angular distributions by explicitly considering the interferences between several outgoing partial waves and by summing over the amplitudes of these exit channels. In this work, the photoelectron peaks observed at a single angle serve as proxies for the true  $\text{NO}^+$  ion rotational state distribution.

Figure 1 demonstrates that the long-range model correctly predicts intensity in all five rotational state channels observed experimentally and reproduces the qualitative intensity pattern. Although a quantitative comparison of the theoretical and experimental intensities is not possible due to the limitations discussed above, it is important to note the significantly reduced intensity of the  $N^+ - R = 0$  channel in both the experimental and theoretical results. Our mechanistically explicit model offers an explanation for this surprisingly weak decay channel. We find that vibrational autoionization into the  $\Delta\ell = 0, N^+ - R = 0$  channel occurs via the quadrupole and polarizability mechanisms with similar magnitudes, but opposite signs. Thus, an interference effect between these

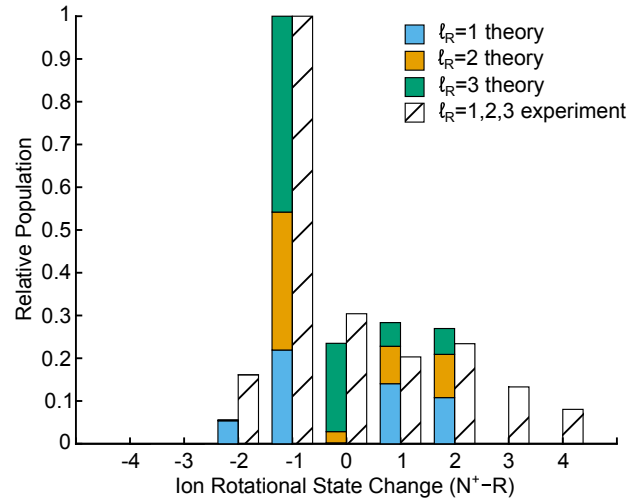


FIG. 2. Rotational state distribution following vibrational autoionization of the unresolved  $13f17_{18,19,20}$  ( $v = 1$ ) states. The experimental data (hatched bars) are the photoelectron peak intensities observed at a single angle, and serve as proxies for the true  $\text{NO}^+$  ion rotational state distribution. The theoretical predictions appear as stacked bars in blue, orange, and green for the  $\ell_R = 1, 2$ , and 3 states, respectively. Both data sets have been normalized by setting the most intense peak to 1. The long-range model predicts a qualitatively correct intensity pattern for ion rotational state changes between  $N^+ - R = -2$  and  $N^+ - R = 2$ , but fails to account for the large rotational state changes of  $N^+ - R = 3$  and 4.

mechanisms suppresses the decay rate into this rotational state channel.

Figures 2 and 3 show the rotational state distributions following vibrational autoionization for the  $\ell_R = 1, 2$ , and 3 states and for the single  $\ell_R = 3$  state, respectively. For the  $\ell_R = 3$  state in Figure 3, the plotted experimental data are the  $\beta_{00}$  parameters from a fit to the measured photoelectron angular distributions, which are directly proportional to the  $\text{NO}^+$  ion yield in that rotational channel. Rotational state distributions for the  $\ell_R = -1, -2$ , and  $-3$  states and the single  $\ell_R = -3$  state have also been analyzed. In both the experimental and theoretical results, these states simply show an inverted rotational state distribution relative to that of the positive  $\ell_R$  states and will not be discussed in further detail.

Our model reproduces the experimental intensity pattern observed in the  $N^+ - R$  channels between  $-2$  and  $2$ . The experimental data for the unresolved  $\ell_R = 1, 2$ , and 3 components display a dominant  $N^+ - R = -1$  peak, a weak  $N^+ - R = -2$  peak and similar intermediate intensity peaks for  $N^+ - R = 0, 1$ , and  $2$ . Our model captures this qualitative pattern, including the weak  $N^+ - R = 2$  peak, which can only be generated via autoionization of the  $\ell_R = 1$  component. The selectively excited  $\ell_R = 3$  data in Figure 3 again displays a dominant  $N^+ - R = -1$  peak. In contrast to Figure 2, no intensity is observed in the  $N^+ - R = -2$  channel because the  $\ell_R = 1$  state is not populated by the laser excitation. In addition, the

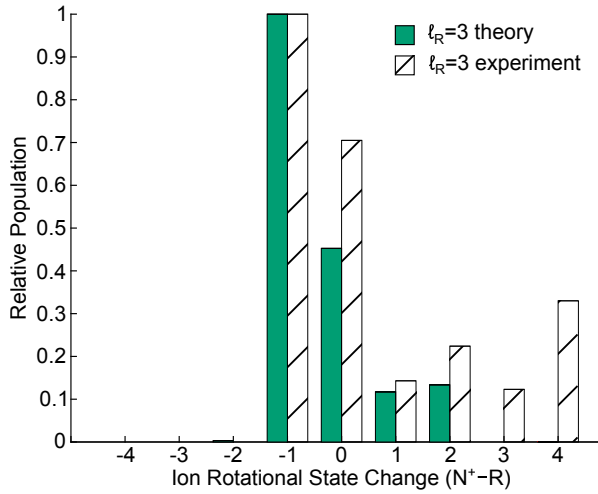


FIG. 3. Rotational state distribution following vibrational autoionization of the single  $11f18_{21}$  ( $v = 2$ ) state. The experimental data (hatched bars) are the  $\beta_{00}$  parameters from a fit to the measured photoelectron angular distributions. These values are directly proportional to the  $\text{NO}^+$  ion rotational state distribution. The theoretical predictions appear in green. Both data sets have been normalized by setting the most intense peak to 1. The long-range model predicts the qualitatively correct intensity pattern for ion rotational state changes between  $N^+ - R = -2$  and  $N^+ - R = 2$ , but fails to account for the large rotational state changes of  $N^+ - R = 3$  and 4.

$N^+ - R = 0$  channel is significantly more intense than the  $N^+ - R = 1$  and 2 channels; this pattern is also captured by our model.

Unlike the  $\ell_R = -1$ , 0, and 1 data set, the experimental results in Figures 2 and 3 show intensity in decay channels  $N^+ - R = 3$  and 4. These decay channels are absent in our model simply because the selection rules for the considered long-range mechanisms (dipole, quadrupole, dipole-dipole polarizability) do not allow for these large changes in angular momentum. We have explored extensions to our model that could produce such large rotational state changes, including higher-order multipoles (octupole, hexadecapole), polarizabilities (dipole-quadrupole, quadrupole-quadrupole, dipole-octupole), and hyperpolarizabilities (dipole-dipole-dipole, dipole-dipole-dipole-dipole). The selection rules for these various mechanisms do allow for large angular momentum changes, and we found that some intensity can be produced in the  $N^+ - R = 3$  and 4 channels. Moreover, the intensity pattern is reversed correctly for  $\ell_R = 3$  versus  $\ell_R = -3$  states. However, the contributions of the higher-order multipoles, the octupole and hexadecapole, were two orders of magnitude lower than those of the dipole, quadrupole, and polarizability. This small contribution is in spite of the fact that the electronic dependence of the octupole scales with distance in the same way as the dipole-dipole polarizability ( $\propto r^{-4}$ ), and results from the weak dependence of these

multipole moments on internuclear distance around the  $\text{NO}^+$  equilibrium bond length.

In addition, the contributions of the higher-order polarizabilities increased unexpectedly and unphysically as the mechanism becomes shorter in range (i.e., as the power  $k$  of the radial matrix element  $\langle r^{-k} \rangle$  increases). In some cases, the intensity pattern for  $|N^+ - R| < 2$  channels was profoundly modified by the addition of a particular higher-order mechanism. We believe this unphysical behavior manifests a breakdown of the fundamental assumption of the long-range model: the Rydberg electron stays sufficiently far from the ion-core that close-range, many-electron interactions can be ignored. The unreasonable intensity of higher-order mechanisms predicted by our model is due mainly to large contributions from  $\ell = 0$  partial waves. For outgoing electron waves with  $\ell = 0$ , and to a lesser extent  $\ell = 1$ , the long-range assumption is not valid. Figure 4 demonstrates this breakdown of the long-range approximation for low- $\ell$  outgoing waves. As the higher-order mechanisms become shorter in range, the integrand is weighted more heavily at small radial distance where low- $\ell$  waves contribute significantly. The  $\text{NO}^+$  internuclear distance of approximately 2 a.u. is represented by a vertical dotted line in Figure 4 and approximates the boundary of the ion-core region, inside of which the long-range approximation is not valid. A phase shift of these low- $\ell$  waves due to close-range, many-electron physics will certainly occur and will significantly change contribution of these channels to autoionization. Since this physics is beyond the scope of our model, we neglect all higher-order electric properties.

This limitation in the current model means that we cannot conclusively eliminate the role of an indirect, electronic mechanism in the vibrational autoionization of NO. Indeed, the  $\ell_R = \pm 3$  states have the greatest partial  $\sigma$  character when projected into a Hund's case (b) basis set. Thus, these states might be expected to interact most strongly with the  $I^2\Sigma^+$  and  $A'^2\Sigma^+$  states that are predominantly responsible for predissociation<sup>17</sup> and an indirect mechanism may contribute to decay channels with large rotational state changes. However, our model also clearly establishes that a direct, vibrational mechanism can account for the majority of the observed rotational decay channels, in spite of the rapid predissociation of  $f$  Rydberg states. This is our most important observation. The faster rate of predissociation than autoionization for  $f$  Rydberg states implies that the bound state coupling to the dissociation continuum is stronger than to the ionization continuum.<sup>26,34</sup> In an indirect autoionization path, a second coupling linking the dissociation and ionization continua is required; our results imply that this continuum-continuum coupling is sufficiently weak as to make this mechanism unimportant for most  $f$  Rydberg states and decay channels studied here. Indeed, previous work points to the prominent role of indirect, predissociation-induced autoionization only in the case of  $|\Delta v| > 1$  decay where the vibrational propensity rule predicts much slower direct, vibrational autoionization.<sup>33</sup>

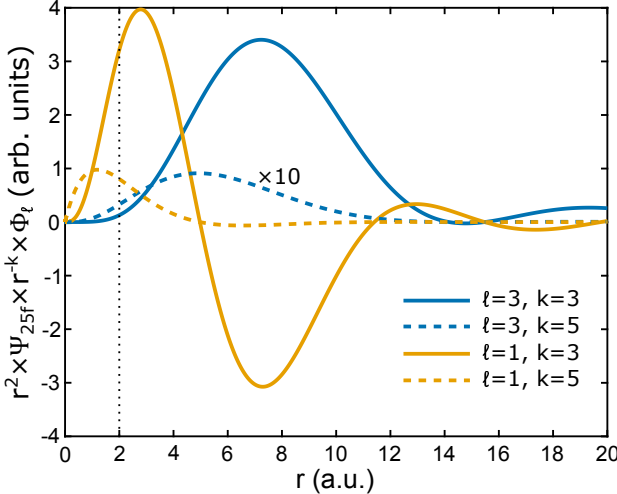


FIG. 4. Integrands of the electronic matrix element as a function of radial distance for a  $25f$  bound Rydberg state and continuum wavefunctions with  $\epsilon = 0.01$  and  $\ell = 1$  or  $3$ . The integrand with  $k = 3$  corresponds to a quadrupole interaction, and  $k = 5$  to a hexadecapole interaction. The  $\ell = 3$ ,  $k = 5$  integrand has been scaled by a factor of 10 for visual clarity. The dotted vertical line at 2 a.u. represents the internuclear distance of  $\text{NO}^+$  and approximates the boundary of the ion-core region. Low- $\ell$  outgoing waves contribute more at short radial distance where the long-range approximation becomes invalid. Higher-order electric properties (larger  $k$ ) weight the integrand heavily at short radial distance, further driving the breakdown of the long-range approximation for low- $\ell$  outgoing waves.

In future work, a more complete theory such as multi-channel quantum defect theory<sup>35,36</sup> will include both the short-range and long-range physics necessary to account for all of these different mechanisms.

### B. Total decay rates of $g$ Rydberg states

Figure 5 shows the experimentally determined total decay rates (solid bars) and theoretical autoionization rates (hatched bars) for the  $22g$  Rydberg state over a range of  $R$  and  $\ell_R$  values. The agreement between the experimental and theoretical values supports the conclusions of previous studies<sup>26</sup>: the non-radiative decay of  $g$  ( $v = 1$ ) states is dominated by autoionization rather than predissociation. These results also stand in stark contrast with the behavior of the  $f$  ( $v = 1$ ) states, which decay predominantly via predissociation at rates orders of magnitude faster than the predicted vibrational autoionization rates of our long-range model. Despite the imperfect selectivity of our preparation scheme, this data set also reveals a pattern of faster autoionization rates for the extreme  $\ell_R$  components of a Rydberg complex, which is in qualitative agreement with the model predictions. In the limit of high rotation, this pattern is explained by the very large decay rates of the  $\Delta\ell = +1$ ,  $N^+ - R = \pm 1$

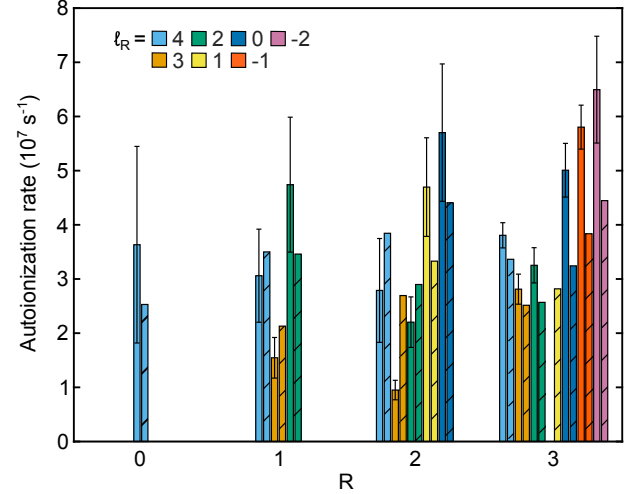


FIG. 5. Experimental total decay rates (solid bars) and theoretical autoionization rates (hatched bars) for the  $22g$  Rydberg state. States with different  $R$  values are labeled on the abscissa and the possible  $\ell_R$  values are shown as different colors with  $\ell_R = 4$  appearing on the left-hand side of each cluster. The error bars reflect the uncertainties of the fit to the raw experimental data.

channels for the extreme  $\ell_R$  states. At the low- $R$  values shown in Figure 5, the pattern is quantitatively different due to the presence of fewer states, but this qualitative pattern persists. Similar agreement between experiment and theory was found for  $25g$  and  $28g$  levels.

### C. Rotational state distributions from autoionization of $g$ Rydberg states

Although no experimental data is available on the  $\text{NO}^+$  ion rotational states accessed by vibrational autoionization of  $g$  states, we have examined the predictions of our long-range model. Given the consistency between the measured total decay rates and the calculated autoionization rates, we anticipate that vibrational autoionization is the dominant decay mechanism for  $g$  states and that our model accurately captures the details of the autoionization dynamics. Figure 6 shows the calculated ion rotational state distributions for all  $\ell_R$  components of the  $25g$  Rydberg states with (a)  $R = 0$ , (b)  $R = 1$ , (c)  $R = 2$ , and (d)  $R = 3$ . The calculated rotational distributions differ significantly from those observed for  $f$  states. Decay into the odd  $N^+ - R = \pm 1$  channels dominates over even  $N^+ - R$  channels. Of particular interest, the  $\ell_R$  components that approach the extreme values of  $\ell_R = 4$  and  $-4$  strongly prefer decay via only the  $N^+ - R = 1$  or  $-1$  channel, respectively. Significantly, several of the individual  $\ell_R$  states (e.g.,  $\ell_R = 3$  for  $R = 1, 2, 3$ ) display a greater than 90% yield of the  $\text{NO}^+$  ion in a single rotational state.

The profound difference in vibrational autoionization dynamics between  $f$  and  $g$  Rydberg states of NO is ex-

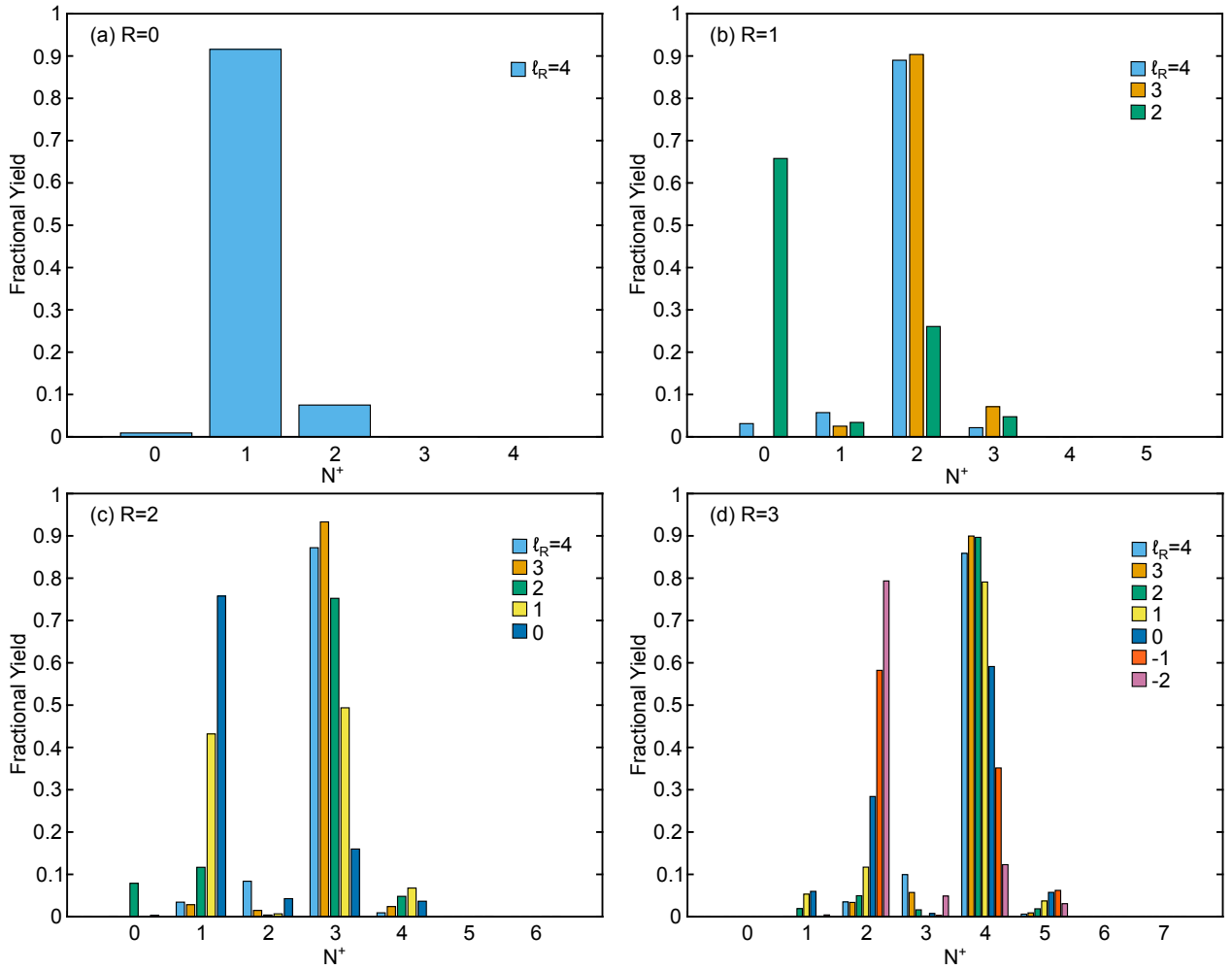


FIG. 6. Ion rotational state distributions following vibrational autoionization of all  $\ell_R$  components of the  $25g$  Rydberg state for (a)  $R = 0$ , (b)  $R = 1$ , (c)  $R = 2$ , and (d)  $R = 3$ . For all states, the dipole mechanism results in decay predominantly via  $N^+ - R = \pm 1$  channels. For specific values of  $\ell_R$ , a greater than 90% yield of the  $\text{NO}^+$  ion in a single rotational level is observed.

plained by the relative strengths of the different long-range mechanisms. Figure 7 shows the relative magnitudes of the matrix elements (see Eq. 3) for the dipole, quadrupole, and polarizability mechanisms averaged over all  $\ell_R$  states and all  $\ell$ ,  $N^+$  decay channels for the  $n = 25$  Rydberg state with different values of  $\ell$ . At low- $\ell$ , the polarizability and quadrupole mechanisms are significantly stronger than the dipole mechanism, reflecting the unusually small dipole moment of the  $\text{NO}^+$  ion-core. As the value of  $\ell$  increases, the centrifugal barrier pushes the Rydberg wavefunction to larger distances,  $r$ , from the ion-core. Since the matrix elements for the dipole, quadrupole and polarizability decrease as  $r^{-2}$ ,  $r^{-3}$ , and  $r^{-4}$ , respectively, the magnitudes of these matrix elements decrease at different rates with increasing  $\ell$ . This results in a re-ordering of magnitudes. For the  $d$  ( $\ell = 2$ ) and  $f$  ( $\ell = 3$ ) states, all three mechanisms contribute to autoionization decay with similar magnitude. This means that  $f$  Rydberg states of NO decay by vibrational

autoionization into all possible ion rotational state channels ( $-2 \leq N^+ - R \leq 2$ ) with significant amplitude. This is reflected in the model predictions shown in Figures 1, 2, and 3. For  $\ell \geq 4$ , the dipole, the longest range mechanism, is nearly an order of magnitude stronger than the other mechanisms. As a result, the two ion rotational state channels ( $N^+ - R = \pm 1$ ) accessed by the dipole mechanism are the dominant decay pathways. As shown in Figure 6, the  $\ell_R = \pm \ell$  states decay preferentially into the channels  $N^+ - R = \pm 1$ , while states with  $\ell_R$  values closer to zero decay into both rotational channels. Since the dipole mechanism is the dominant mechanism for all states with  $\ell \geq 4$ , this pattern in the vibrational autoionization decay dynamics is expected to occur for all high- $\ell$  Rydberg states of NO and all other heteronuclear diatomic molecules.

This universal vibrational autoionization behavior makes high- $\ell$  Rydberg states attractive targets for state-selective production of molecular ions. Seven

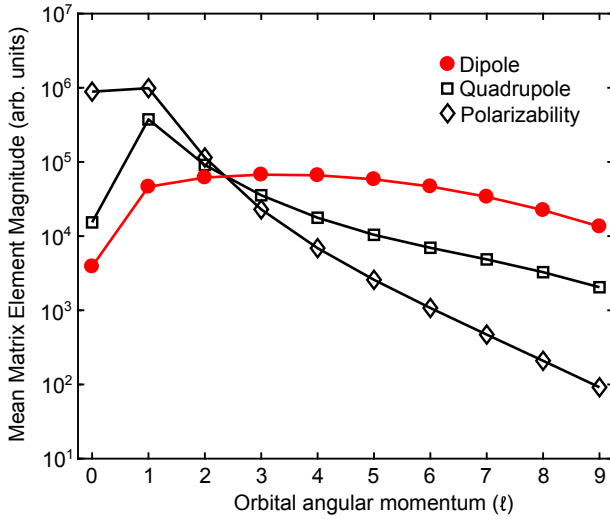


FIG. 7. Matrix elements calculated according to Eq. 3 for the dipole, quadrupole, and polarizability mechanisms averaged over all  $\ell_R$  components and all  $\ell$ ,  $N^+$  decay channels of the  $n = 25$  Rydberg state as a function of the Rydberg electron orbital angular momentum  $\ell$ . For  $d$  and  $f$  states, all three mechanisms contribute similarly to vibrational autoionization resulting in population of many ion rotational states. As the value of  $\ell$  increases the magnitudes of the quadrupole and polarizability mechanisms decrease rapidly. The long-range dipole mechanism dominates the decay dynamics for all high- $\ell$  states.

eral experiments in precision measurement<sup>9,37</sup> and cold chemistry<sup>6,38</sup> require molecular ions in a single quantum state, but typical methods of ion production (e.g., discharge, laser ablation) are violent and produce ions in numerous quantum states. In contrast, autoionization of Rydberg states has been used in a few previous experiments<sup>8,9</sup> to generate molecular ions in only a few quantum states, greatly increasing the yield of the desired state and reducing the complexity of subsequent state preparation steps. The calculated rotational state distributions presented here demonstrate that greater selectivity in the generation of single quantum state ions is possible by careful selection of high- $\ell$  Rydberg states as the precursor to autoionization. New methods for the preparation of high- $\ell$  Rydberg states<sup>39,40</sup> will be important for exploitation of this approach.

## V. CONCLUSION

We have examined the predictions of a long-range model for vibrational autoionization of NO and have validated the simplified physical mechanisms of this model by comparison with experimental data for Rydberg states with  $\ell = 3$  and 4. We find that the long-range model predicts NO<sup>+</sup> rotational state distributions that result from autoionization of  $f$  levels that are largely consistent with the experimental observations.<sup>10,11,13</sup> The agreement is

particularly striking for states with  $|\ell_R| \leq 1$ . The extreme  $\ell_R$  components decay by additional  $N^+ - R = \pm 3$ , and  $\pm 4$  channels, which are not captured by our model. Future extensions of the long-range model to include higher-order polarizabilities and explicit phase shifts due to core-penetration, or application of multichannel quantum defect theory will account for these discrepancies. While we cannot conclusively rule out any contribution from indirect predissociation-mediated autoionization, our results strongly support direct, vibrational autoionization as the dominant mechanism.

Non-radiative lifetimes of  $g$  Rydberg states of NO have been directly measured by delayed pulsed field extraction of NO<sup>+</sup> ions resulting from autoionization. We find good agreement between the experimental total decay rates and the autoionization rates predicted by our long-range model, though the calculated rates are generally slower than the observed rates. Significantly, the non-radiative decay of  $g$  states is dominated by autoionization rather than predissociation, in contrast with the behavior of all low- $\ell$  Rydberg states of NO.

Finally, we propose that vibrational autoionization of selected  $g$  Rydberg states is an efficient strategy for producing molecular ions in single selected quantum states. While our investigation focuses on NO, this experimental and theoretical methodology will be applicable to a variety of molecules because high- $\ell$  Rydberg states obey a universal scaling of the long-range autoionization mechanisms. Efficient production of quantum-state selected ions is desirable for diverse applications in precision measurement,<sup>9,37</sup> cold chemistry,<sup>6,38</sup> and quantum computing.<sup>41</sup>

## DATA AVAILABILITY

The data that support the findings of this study are available from the corresponding author upon reasonable request.

## ACKNOWLEDGMENTS

We gratefully acknowledge insightful conversations with Ed Eyler (University of Connecticut) and Heather Lewandowski (University of Colorado/JILA) that inspired this work. This material is based on work supported by the National Science Foundation, under Award No. CHE-1800410 and the AFOSR, under Award No. FA9550-16-1-0117. T.J.B. was supported by the National Science Foundation Graduate Research Fellowship Program under Grant No. 1122374. J.J. assisted in the preparation of this manuscript at Lawrence Livermore National Laboratory under the auspices of the U.S. Department of Energy under Contract DE-AC52-07NA27344.

<sup>1</sup>B. K. Stuhl, M. T. Hummon, and J. Ye, Annual Review of Physical Chemistry **65**, 501 (2014).

<sup>2</sup>B. R. Heazlewood and T. P. Softley, *Nature Reviews Chemistry* **5**, 125 (2021).

<sup>3</sup>J. Toscano, H. J. Lewandowski, and B. R. Heazlewood, *Physical Chemistry Chemical Physics* **22**, 9180 (2020).

<sup>4</sup>Y. Liu, M.-G. Hu, M. A. Nichols, D. D. Grimes, T. Karman, H. Guo, and K.-K. Ni, *Nature Physics* **16**, 1132 (2020).

<sup>5</sup>M.-G. Hu, Y. Liu, M. A. Nichols, L. Zhu, G. Quéméner, O. Dulieu, and K.-K. Ni, *Nature Chemistry* **13**, 435 (2021).

<sup>6</sup>X. Tong, T. Nagy, J. Y. Reyes, M. Germann, M. Meuwly, and S. Willitsch, *Chemical Physics Letters* **547**, 1 (2012).

<sup>7</sup>M.-G. Hu, Y. Liu, D. D. Grimes, Y.-W. Lin, A. H. Gheorghe, R. Vexiau, N. Bouloufa-Maafa, O. Dulieu, T. Rosenband, and K.-K. Ni, *Science* **366**, 1111 (2019).

<sup>8</sup>Y. Zhou, K. B. Ng, L. Cheng, D. N. Gresh, R. W. Field, J. Ye, and E. A. Cornell, *Journal of Molecular Spectroscopy* **358**, 1 (2019).

<sup>9</sup>H. Loh, J. Wang, M. Grau, T. S. Yahn, R. W. Field, C. H. Greene, and E. A. Cornell, *The Journal of Chemical Physics* **135**, 154308 (2011).

<sup>10</sup>H. Park, D. J. Leahy, and R. N. Zare, *Physical Review Letters* **76**, 1591 (1996).

<sup>11</sup>H. Park and R. N. Zare, *The Journal of Chemical Physics* **106**, 2239 (1997).

<sup>12</sup>I. Konen, R. Zhao, and R. N. Zare, in *Dissociative Recombination of Molecular Ions with Electrons*, edited by S. L. Guberman (Kluwer Academic/Plenum Publishers, 2003).

<sup>13</sup>R. Zhao, *Vibrational autoionization from  $nf$  Rydberg states of nitric oxide*, Ph.D. thesis, Stanford University (2004).

<sup>14</sup>E. Miescher and K. P. Huber, in *International Review of Science, Physical Chemistry Series 2, Volume 3. Spectroscopy*, edited by A. D. Buckingham (Butterworths, London, 1976).

<sup>15</sup>S. Fredin, D. Gauyacq, M. Horani, C. Jungen, G. Lefevre, and F. Masnou-Seeuws, *Molecular Physics* **60**, 825 (1987).

<sup>16</sup>W. Y. Cheung, W. A. Chupka, S. D. Colson, D. Gauyacq, P. Avouris, and J. J. Wynne, *The Journal of Chemical Physics* **78**, 3625 (1983).

<sup>17</sup>S. T. Pratt, *The Journal of Chemical Physics* **108**, 7131 (1998).

<sup>18</sup>A. Russek, M. R. Patterson, and R. L. Becker, *Physical Review* **167**, 17 (1968).

<sup>19</sup>E. E. Eyler, *Physical Review A* **34**, 2881 (1986).

<sup>20</sup>E. E. Eyler and F. M. Pipkin, *Physical Review A* **27**, 2462 (1983).

<sup>21</sup>F. Neese, *Wiley Interdisciplinary Reviews: Computational Molecular Science* **2**, 73 (2012).

<sup>22</sup>F. Neese, *Wiley Interdisciplinary Reviews: Computational Molecular Science* **8**, e1327 (2017).

<sup>23</sup>M. Fehér and P. A. Martin, *Journal of the Chemical Society Faraday Transactions* **91**, 1063 (1995).

<sup>24</sup>D. T. Colbert and W. H. Miller, *The Journal of Chemical Physics* **96**, 1982 (1992).

<sup>25</sup>S. A. Bhatti, C. L. Cramer, and W. E. Cooke, *Physical Review A* **24**, 161 (1981).

<sup>26</sup>A. Fujii and N. Morita, *The Journal of Chemical Physics* **103**, 6029 (1995).

<sup>27</sup>J. J. Kay, D. S. Byun, J. O. Clevenger, X. Jiang, V. S. Petrović, R. Seiler, J. R. Barchi, A. J. Merer, and R. W. Field, *Canadian Journal of Chemistry* **82**, 791 (2004).

<sup>28</sup>M. J. J. Vrakking and Y. T. Lee, *The Journal of Chemical Physics* **102**, 8818 (1995).

<sup>29</sup>E. Murgu, J. D. D. Martin, and T. F. Gallagher, *The Journal of Chemical Physics* **115**, 7032 (2001).

<sup>30</sup>M. J. J. Vrakking, *The Journal of Chemical Physics* **105**, 7336 (1996).

<sup>31</sup>V. S. Petrović and R. W. Field, *The Journal of Chemical Physics* **128**, 014301 (2008).

<sup>32</sup>G. Herzberg, *Molecular Spectra and Molecular Structure. Vol I. Spectra of Diatomic Molecules* (D. Van Nostrand Company, Inc., New York, 1950).

<sup>33</sup>A. Giusti-Suzor and C. Jungen, *The Journal of Chemical Physics* **80**, 986 (1984).

<sup>34</sup>A. Fujii and N. Morita, *The Journal of Chemical Physics* **97**, 327 (1992).

<sup>35</sup>C. Jungen and S. C. Ross, *Physical Review A* **55** (1997).

<sup>36</sup>J. Jiang, T. J. Barnum, S. L. Coy, and R. W. Field, *The Journal of Chemical Physics* **150**, 154305 (2019).

<sup>37</sup>M. Germann, X. Tong, and S. Willitsch, *Nature Physics* **10**, 820 (2014).

<sup>38</sup>P. C. Schmid, M. I. Miller, J. Greenberg, T. L. Nguyen, J. F. Stanton, and H. J. Lewandowski, *Molecular Physics* **117**, 3036 (2019).

<sup>39</sup>A. A. Morgan, V. Zhelyazkova, and S. D. Hogan, *Physical Review A* **98**, 043416 (2018).

<sup>40</sup>T. J. Barnum, H. Herburger, D. D. Grimes, J. Jiang, and R. W. Field, *The Journal of Chemical Physics* **153**, 048301 (2020).

<sup>41</sup>D. I. Schuster, L. S. Bishop, I. L. Chuang, D. DeMille, and R. J. Schoelkopf, *Physical Review A* **83**, 012311 (2011).